Max Ovenden
Department of Engineering,
Durham University,
South Road, Durham, DH1 3LE, UK
e-mail: movenden@scottlogic.com

Qing Wang[1]
Department of Engineering,
Durham University,
South Road, Durham, DH1 3LE, UK
e-mail: Qing.wang@durham.ac.uk

Songling Huang
State Key Laboratory of Power System,
Department of Electrical Engineering,
Tsinghua University,
Beijing 100084, China
e-mail: huangsling@tsinghua.edu.cn

Wei Zhao
State Key Laboratory of Power System,
Department of Electrical Engineering,
Tsinghua University,
Beijing 100084, China
e-mail: zhaowei@tsinghua.edu.cn

Shen Wang
State Key Laboratory of Power System,
Department of Electrical Engineering,
Tsinghua University,
Beijing 100084, China
e-mail: wangshen@mail.tsinghua.edu.cn

Real-Time Monitoring of Wind Turbine Blade Alignment Using Laser Displacement and Strain Measurement

Wind turbine (WT) blade structural health monitoring (SHM) is important as it allows damage or misalignment to be detected before it causes catastrophic damage such as that caused by the blade striking the tower. Both of these can be very costly and justify the expense of monitoring. This paper aims to deduce whether a SICK DT-50 laser displacement sensor (LDS) installed inside the tower and a half-bridge type II strain gauge bridge installed at the blade root are capable of detecting ice loading, misalignment, and bolt loosening while the WT is running. Blade faults were detected by the virtual instrument, which conducted a z-test at 99% and 98% significance levels for the LDS and at 99.5% and 99% significance levels for the strain gauge. The significance levels chosen correspond to typical Z-values for statistical tests. A higher significance was used for the strain gauge as it used a one-tail test as opposed to a two-tail test for the LDS. The two different tests were used to test for different sensitivities of the tests. The results show that the strain gauge was capable of detecting all the mass loading cases to 99.5% significance, and the LDS was capable of detecting misalignment, bolt loosening, and 3 out of 4 mass loading cases to 99% significance. It was able to detect the least severe mass loading case of 11 g at the root to only a 98% significance. [DOI: 10.1115/1.4043850]

1 Introduction

Wind turbine (WT) technology has been gaining prevalence recently due to an increasing global demand for energy and fears about environmental damage. According to the Global Wind Energy Council [1], in 2016 more than 54 GW of clean renewable wind power was installed across the global market across 16 countries, increasing the total capacity to 487 GW—a 12.6% increase. On top of this, they predict it will almost double to 800 GW by the end of 2021. This is due in part to environmental awareness and decreasing cost but also due to government policies aimed at increasing renewable energy use—such as the European Union (EU) aiming to increase renewable use to 20% in the year 2020 [2].

In order for the WT industry to live up to the targets and predictions, the key focus is on reducing operating costs while maintaining safety and reliability. Wind turbines must deal with rain, thunder, high winds, and even ice. These create fatigue and can cause problems such as misalignment and cracks [3,4]. This can be costly in reducing the efficiency of the turbine and can also lead to more serious failures that can be costly to remedy and create significant downtime involving dangerous repair work. Additionally, recent installations have been of larger turbines [5], which, along with rising fabrication costs, makes repair and downtime more expensive. Larger blades also mean larger tip deflections making tower strikes by the blade at high winds more likely. These are catastrophic and must be avoided at all costs.

Structural health monitoring (SHM) is a nondestructive method of detecting and classifying defects and damage to engineering structures through sensors and data transmission [6,7]. Through SHM, any problems can be detected in real-time and can be addressed quickly before escalation. Studies have shown the economic benefits of SHM; only 47% of all major failure events need to be prevented through maintenance to make SHM economically viable [8] because of the expensive nature of repair work and the relatively low cost of the monitoring equipment.

In this paper, the main methods by which SHM is employed in the industry, and several potential innovations, are outlined. From the literature review, an experimentation plan on a small WT model is justified and carried out. This plans to assess the feasibility of a laser displacement sensor (LDS) built into the tower and a half-bridge type II strain gauge bridge attached to the blade. From the literature, we have found Berndt et al. [9] used a full-bridge circuit configuration for operation in autonomous wireless condition monitoring systems. In Loraux and Brühwiler's paper [10], the quarter configuration of the circuit is chosen, and the signal is postprocessed to remove the temperature effects. This provides optimal solutions in terms of sensors for evaluation of the future service duration of the wind turbine. No previous studies to our knowledge have used type II half-bridge gauges for monitoring wind turbine blades despite their lower cost compared with other bridge configurations. Real-time monitoring is to be achieved using a virtual instrument (VI) built using National Instruments' LABVIEW program. A *z*-test was incorporated in the LABVIEW VIs for both the LDS and strain gauge, allowing error warnings to be displayed in real-time. The hypotheses that were tested were that the average strain was higher than expected and that the average displacement measured for each blade was higher or lower than expected at 98% and 99% significance. The tests were conducted for the detection of ice loading, bolt loosening, and misalignment by the LDS and of ice loading by the strain gauge.

[1]Corresponding author.

Manuscript received December 2, 2018; final manuscript received May 20, 2019; published online June 6, 2019. Assoc. Editor: Hoon Sohn.

2 Current Wind Turbine Monitoring Trends

2.1 Laser Measurement. A LDS uses either triangulation or time-of-flight principles to measure the distance of a surface from the laser source. Triangulation is when the reflected laser is deflected by an angle before reaching a detector. From this deflection angle, trigonometry can be used to calculate the distance at which the laser is reflected. Time-of-flight LDSs record the time taken for the laser beam to travel from the source and be reflected back. Using the speed of light, the distance the laser beam traveled can be calculated and divided in two to obtain the distance at which it is reflected. Several studies in labs have been conducted to show detection capabilities of an LDS for misalignment, bolt loosening, nacelle tilt, and extra mass on the blade (due to ice buildup) or mass loss from the blade (caused by lightning) [11–14]. Singh [12], Flanagan [13], and Todd [14] used a SICK DT50 LDS sensor to successfully detect these faults, and Kim [11] et al. and Lee and Kim [15] used an OMRON-3Z4M to detect these faults and recommended using a SICK DT50 due to its superior range, which is suitable for measuring larger WT blades such as the 2-MW Vestas blade. The previously mentioned studies substantiate this claim on small-scale tests in a lab. However, in these studies, the LDS was positioned horizontally along the blade as if next to the tower, an unrealistic location for an actual WT. A better position for it would be vertically below the axis of rotation, as if attached to the WT tower. This is the position in which it is most common for an LDS to be placed in a real wind turbine, which is also the LDS position that we selected in this paper.

2.2 Strain Measurement. The most common method of strain measurement is by using metallic strain gauges. These consist of a strip of metallic foil bonded to a measuring surface that experiences a change in resistance linearly in response to an applied strain. The constant of proportionality between the strain and this change is called the gauge factor (*GF*) and is given by the following equation [16]:

$$GF = \frac{\Delta R/R}{\Delta L/L} \tag{1}$$

where L and ΔL are the original and change in lengths, respectively, and R and ΔR are the original and change in resistance, respectively. When this gauge replaces a resistor on a Wheatstone bridge, the output voltage changes in proportion to the change in resistance and, therefore, strain.

Several different configurations of strain gauges are possible for different applications. Bridges can have one, two, or four strain gauges and are referred to as quarter-, half-, and full-bridge gauges, respectively. For each of these, there are distinct types, which involve changing the orientation of the gauges on the surface. In general, the more strain gauges, the more sensitive the bridge—meaning a higher signal-to-noise ratio. National Instruments summarizes each configuration including its effect on error due to both temperature and Poisson's effect [16]. A full-bridge type I has a sensitivity of 1.3 mV/V and compensates for both temperature and Poisson's effect. A half-bridge type II has a slightly lower sensitivity of 1.0 mV/V and compensates for temperature effects only. Fewer strain gauges are required for half-bridge configurations and even less so for quarter bridges. This results in them being significantly less costly to install.

Metallic strain gauges are also sensitive to magnetic fields. When in the presence of a time-varying magnetic field, such as that of a generator, a voltage can be induced in the wires causing unwanted noise. This can be controlled by using twisted lead wires and minimizing the sizes of the loops on either side of the bridge [17]. The error that occurs through changes in temperature is the most common in strain measurement and, although the use of compensated gauges can significantly reduce it, there can still often be a residual error of about 10×10^{-3} strain per degree Celsius [18].

Bezziccheri et al. [19] go into more detail about different external effects on the calibration and accuracy of strain gauges on wind turbine blades and outline the difficulty in applying a known load on large-scale WT blades for accurate calibration as well as describing a model to provide reference loads using unbalanced structural masses. The extent of temperature differentials is highlighted by solar imaging of WT blades as well as temperature sensors near the gauges on the blades showing differentials of up to 20 deg. This arises from both solar heating and mechanical heating from components. Because of this, they recommend calibration at night, when the solar heating effect from the sun is at its lowest, and the use of full-bridge strain gauges because of their linearity and high sensitivity, in particular, a type-T gauge for measuring bending strain. A type-T gauge is a full-bridge strain gauge in which each side of the blade has two gauges in perpendicular directions, as shown in Fig. 1. When one side of the blade measures positive strain, the other side measures negative strain. Therefore, if the two sides of the blade have similar thermal expansion rates, the two changes in strain will cancel out the net effect.

Papadopoulos et al. [20] also recommends this configuration and maintains that temperature is the most significant source of error, especially in composite blades that exhibit anisotropy in stiffness and thermal expansion coefficients. This gauge configuration was used to conduct accurate mass loading detection on small model WT blades in a controlled lab setting by Flanagan [13].

Aihara et al. [21] proposed a strain-based vibration monitoring system using strain gauges. It used modal analysis to accurately estimate the vibration in the direction that would result in the blade hitting the tower. Two single-strain gauges were used, and the voltages were amplified and passed through an analog-to-digital converter before data processing. They concluded that the deflection estimation accuracy is good enough for practical use. Lee et al. [22] proposed a similar strain-based system for measuring blade deflection using the linear correlation of blade deflection with the strain measured by three strain gauges connected to a strain logger. They determined the optimal positioning for the strain gauges on a 0.75-m long blade to be at 0.1 m and 0.45 m from the root. This gave satisfactory results that were congruous with those of direct measurement using laser displacement sensors. These studies show that good results can be obtained with single-strain gauges without a full-bridge configuration.

Fiber Braggs grating (FBG) is an optical strain measurement technique. It utilizes pieces of optical fiber with localized differences in refractive index [23]. Just like metallic gauges, these are sensitive to temperature, and so, multiple gratings are required to compensate for this. When a light source is applied at one end, the wavelength of the refracted light changes in proportion to the strain applied. Compared with strain gauges, FBG sensors have a higher immunity to electrical noise, do not require external excitation, and are highly resistant to corrosion [24]. This makes them ideal for situations involving submersion in water, such as in a paper by Mieloszyk and Ostachowicz [25] in which a water basin and a wave machine were used to simulate an environmental load, and FBG was able to detect the appearance of circumferential cracks on a wind turbine support structure. WT blades, however, are clearly not subject to such great corrosive and environmental pressures. Research into its use for WT blade monitoring is limited. Park et al. [26] used FBG sensors to accurately detect yawing, pitching, and normal operating conditions, although they did not show their ability to detect damage such as blade misalignment. It is evident

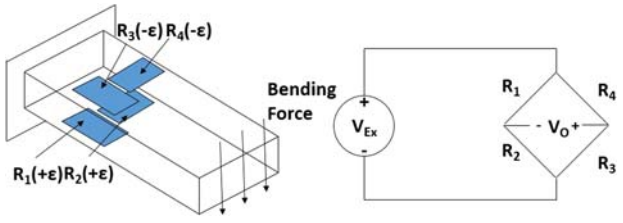

Fig. 1 Strain gauge positions and wiring of a type-T Bridge

that the benefits that FBG sensors hold do not justify their increased cost for WT blade monitoring.

An interesting new technology application in the field of strain measurement utilizes piezo-electric sensors. These make use of a crystal that releases a charge proportional to an applied pressure or temperature that allows the strain to be determined. They have a high stiffness and resonant frequency dependent on the size of the crystal used. For example, a transducer with a 0.5-in. diameter has a resonant frequency of 5 MHz, and, using a different crystal, a resonant frequency of up to 20 MHz can be achieved [27]. This makes them good for accurately measuring small forces. However, large forces limit the bandwidth, so strain gauges are better at measuring large forces at a slower rate [28]. Piezo-electric sensors also have a drift of 60 N/h, which makes them unsuitable for measurements over a large period of time such as in real-time SHM that takes place continuously throughout the WT operation. However, Lim et al. [29] proposed a monitoring algorithm using piezosensors charging capacitors on each blade that sends a pulse when full before discharging. Given that the size and stiffness of the gauges on each blade are the same, the blades will experience roughly the same strain energy over time, and the pulses will be sent at the same time. Any mismatch between the timing of these pulses on each blade indicates the presence of blade damage without the use of any computational model of the turbine. This method takes advantage of the fact that when the blades' strain energies are being compared, the electric drift on each sensor is compensated for. As far as the research shows, however, a similar system for measuring misalignment has not yet been realized; this is a possibility for the future research.

3 Method

3.1 Experimental Setup. The WT was an AIR Breeze turbine manufactured by Primus Windpower Inc. It has three blades and a rotor diameter of 1.15 m [30].

The WT was driven by an electrical motor powered by a 6-V input, driving the blades at a speed of around 16 rpm. Lee and Kim [15] used data from a full-scale 50-m long blade to determine that speeds of 20–30 rpm are common. Other experiments on smaller scale blades have used speeds of 12 rpm [12,14]. Due to the smaller nature of the blade used here and limitations of the motor, a speed of 16 rpm was chosen.

For both the strain gauge and LDS, the output voltage is wired through a NI USB—6281 input–output box and connected to the PC by USB. A block diagram of the lab setup for both LDS and strain measurements is shown in Fig. 2.

Data are then acquired through LABVIEW software designed by National Instruments™, which is used to create VIs with which data are acquired, processed, and can be displayed to a user in real-time and stored. Separate VIs are created for the real-time monitoring of the strain gauges and the LDS.

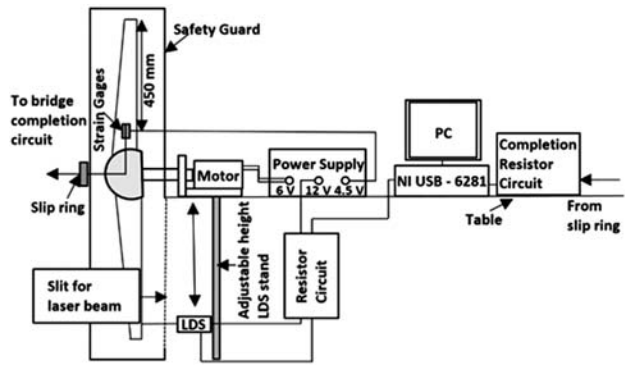

Fig. 2 Block diagram of the lab setup for both LDS and strain measurements

3.2 Simulation of Blade Faults. All of these tests involve damage to blade 1. For mass loading, based on the setting of the LDS and strain measurement, blade 1 was loaded with a 45-g mass at the root (450 mm from the blade tip) and an 11-g mass at the root, middle, and end of the blade (450 mm, 250 mm, and 50 mm from the blade tip, respectively). The loading scenarios including the unloaded case are summarized in Table 1, with each case numbered for reference. The loading cases are numbered such that the higher the case number, the greater the severity of the mass loading. Case 4 involves the most severe loading possible while still allowing the blades to be driven by the motor. The motor failed to drive the blade when the 45-g mass was attached to either the middle or the end of the blade.

The masses were attached centrally across the width of the blade, and the distances indicated above refer to the distance from the tip to the center of the attached masses.

To simulate misalignment, washers were measured by a digital caliper and placed between the blade and the hub. Washers were added sequentially, and the combined thickness of the washers between the hub and blade was taken as the value of blade misalignment.

Bolt loosening was simulated by turning the nut that holds the blade in place by a set number of turns. Two nuts were used in order to assure that the movement of the blade did not cause the already loose nut to loosen further. Each turn of the nut was measured to correspond to an extra 1 mm of extra space for the blade to move.

3.3 Statistical Verification of Faults. A hypothesis test is used in order to tell whether or not an increase or decrease in strain or displacement is significant. The test used in this experiment is the z-test as it is appropriate for large sample sizes of at least 30. Due to the relatively high sample rate used, the strain gauge running for 30 s at a 10 Hz sample rate generates a sample of 300 data points and the LDS running for 15 full-blade rotations generates between 70 and 113 data points per blade. This is sufficient to assume that sample means are normally distributed due to the central limit theorem. The z-test is therefore appropriate in these experiments.

Given a sample of sufficient size, this tests whether to accept or reject a null hypothesis H_0 that the actual population mean μ is unchanged from the assumed population mean μ_0. This is expressed by

$$H_0 : \mu = \mu_0 \tag{2}$$

This is tested against an alternative hypothesis H_1, which for the LDS is that the actual mean is not equal to the assumed mean—a two-tail test as the test must distinguish between each blade being either too close or too far from the mean. This is expressed by

$$H_1 : \mu \neq \mu_0 \tag{3}$$

For the strain gauge, the alternative hypothesis is that the actual mean is larger than the assumed mean—a one-tail test as it does not matter if the strain is lower than the expected—and is expressed by

$$H_1 : \mu > \mu_0 \tag{4}$$

The significance level of the test is given by $1 - \alpha$, where α is the probability of incorrectly rejecting H_0. The higher the significance level, the more confidently the null hypothesis can be rejected.

Table 1 Summary of each mass loading case

Distance from tip (mm)	Case 0	Case 1	Case 2	Case 3	Case 4	Mass ratio of load and blade
50 (end)	0 g	0 g	0 g	11 g	0 g	0.55
250 (middle)	0 g	0 g	11 g	0 g	0 g	0.55
450 (root)	0 g	11 g	0 g	0 g	45 g	2.25

The following equation gives a z-value for a given sample mean [31]:

$$z = \frac{\bar{x} - \mu_0}{\sigma/\sqrt{n}} \tag{5}$$

where $\bar{x}$ is the sample mean, σ is the population standard deviation, and n is the sample size. This represents where the sample mean lies on the standard normal distribution of the mean equal to zero and standard deviation equal to 1. The critical z-values chosen are ± 2.326 and ± 2.576 for the LDS, and for the strain gauge, just the positive values are taken, as it is a one-tail test. These correspond to significance levels of 98% and 99% for the LDS and of 99% and 99.5% for the strain gauge. Critical values are given in a standard z-table. If the calculated z-value falls outside of this range then H_0 can be rejected with the corresponding level of certainty.

The display of error is shown in the VI front panel, which tells the user when damage is detected with these levels of significance and displays an appropriate warning of an error in the form of light-emitting diode (LEDs).

3.4 Strain Gauge. A half-bridge type II was setup at the root of the blade, 450 mm from the blade tip. This position was chosen because given any load at any point across the blade, there will be a higher bending moment, and therefore strain at the root, furthest from the tip. This gauge consists of two strain gauges and two completion resistors making up a Wheatstone bridge circuit, as shown in Fig. 3.

The strain was calculated from the output voltage by first calculating a reference voltage V_r from the difference between the strained and unstrained output and input voltage ratios. This is expressed in the following equation [32]:

$$V_r = \left(\frac{V_{out}}{V_{ex}}\right)_{Strained} - \left(\frac{V_{out}}{V_{ex}}\right)_{Unstrained} \tag{6}$$

where V_{out} and V_{ex} refer to the voltage output from the strain gauge and the strain gauge excitation voltage, respectively. Assuming negligible lead wire resistance, this is then used to calculate the strain ϵ, using the known GF and with the equation

$$\varepsilon = \frac{-2V_r}{GF} \tag{7}$$

The gauge factor of the strain gauges used for this experiment is equal to 2.1, as is typical for metallic strain gauges [15].

The value of the excitation voltage V_{ex} to be used is recommended by National Instruments™ to be between 3 V and 10 V [33]. A value of around 4.5 V is chosen to minimize error from ohmic heating as a compromise against the signal-to-noise ratio. One of the main sources of noise is that created by an unstable voltage source. This is evident from Fig. 4, which shows the strain output when a constant value of $V_{ex} = 4.5$ is used in Eq. (6) for calibration. The peaks and troughs of V_{ex} roughly correspond to the peaks and troughs of the strain measured.

This error can be considerably reduced by measuring V_{ex} in real-time, as it varies, and using this value in Eq. (6) in the VI instead.

For the strain gauge, only mass loading was tested for as bolt loosening and misalignment do not change the load that the blade experiences. Previous studies with gauges of higher sensitivities have shown this to be the case by showing failure in detecting these faults with strain gauges [14].

Two different VI programs were used to detect faults. One calculated the strain using the relatively noisy V_{out} and V_{ex} data and Eqs. (6) and (7). The second calculated the triangular moving average of 20 data points of both V_{out} and V_{ex} data before the strain calculations.

The data flow diagrams for the filtered case are shown in Fig. 5. For the unfiltered case, the same process is followed but the triangular moving average is not calculated in the third stage.

For both of these, the unstrained V_{out}/V_{ex} is calculated first from an unloaded blade at rest over a period of 420 s. The assumed population mean μ_0 and standard deviation σ is then calculated for an unloaded blade running at 16 rpm (normal operating conditions) by calculating the average strain over a long period of time—2100 s for the unfiltered case and 320 s for the filtered case. Because of the noise partly being filtered, the amount of data required to get an accurate representation of the population data is less than for the unfiltered case.

The values of the average unstrained voltage ratios, the average population strains, and population standard deviations that are used in the VIs are shown in Table 2. Filtering the data using triangular moving averages can reduce the standard deviation to less than half that of the unfiltered case while increasing the average strain measured. This is equivalent to increasing the signal-to-noise ratio and so the filtered case is predicted to be the better predictor.

3.5 Laser Displacement Sensor. The LDS used in this project is a SICK DT50-P1113, as recommended by Lee et al. [14], because it has a range of 10,000 mm and an accuracy of ±10 mm [34] and so is suitable for measuring large-scale WTs. Figure 6 below shows how the LDS is wired up. The 12 V input is supplied by a power supply and the output voltage goes to the personal computer.

The range was manually adjusted between 200 mm and 400 mm, giving an output of between 4 mA and 20 mA. The 270 Ω resistor wired in parallel to the output gives corresponding output voltage ranges of between 1.08 V and 5.40 V, respectively. As the output voltage varies linearly between these two values as the distance

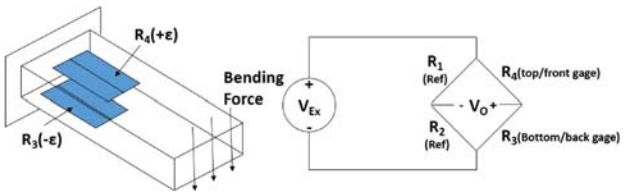

Fig. 3 Strain gauge positions and wiring of a type II half-bridge

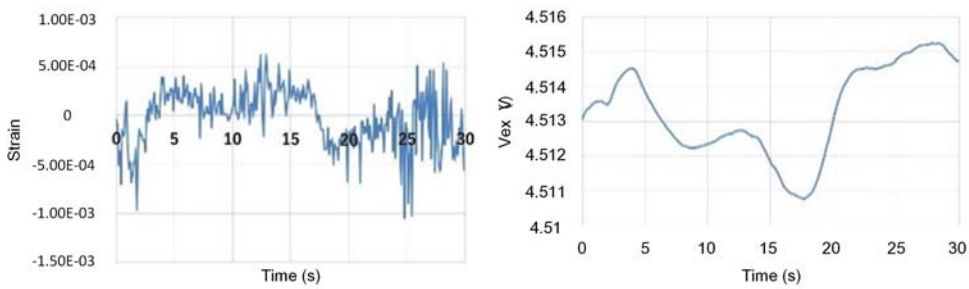

Fig. 4 Strain output for constant V_{ex} used in VI (left) and the corresponding V_{ex} measured (right) for a 30-s sample

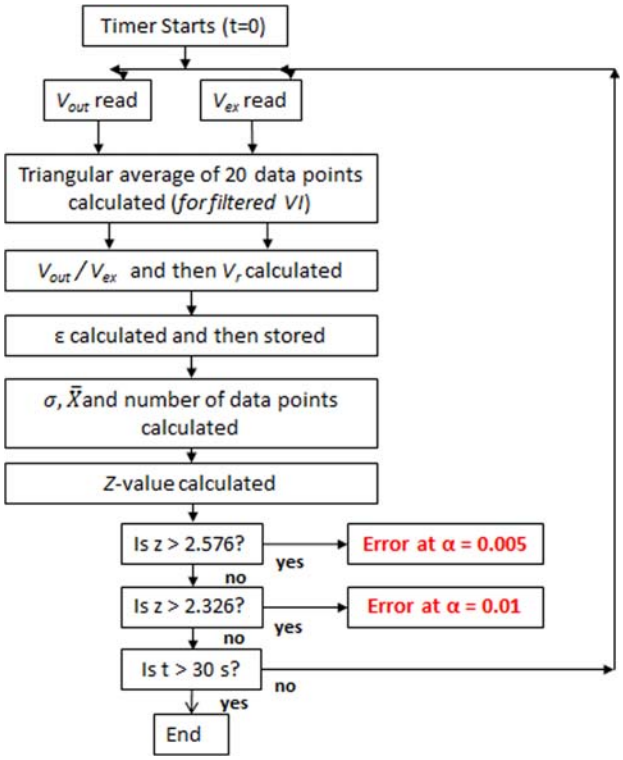

Fig. 5 Flow diagram of the VI with hypothesis testing during one 30 s sample

Table 2 Values of the average unstrained voltage ratios, the average population strains, and population standard deviations that are used in the VIs for the hypothesis test

	$\left(\frac{V_{out}}{V_{ex}}\right)_{Unstrained}$	Population mean strain, μ_0	Population standard deviation, σ
Filtered case	0.4996	5.823×10^{-5}	1.154×10^{-4}
Unfiltered case	0.4995	3.893×10^{-5}	2.557×10^{-4}

varies between 200 mm and 400 mm, the displacement d is calculated from the voltage measured V_{LDS} using

$$d = 46.296 \times V_{LDS} + 150 \quad (8)$$

Using LABVIEW, a VI was created to convert the output voltage into a distance in millimeters and record the data across a period of time. It also calculates statistics and carries out a two-tail z-test for each blade, telling the user if the blade is too far or too close with a 98% and 99% significance level. The process is outlined in a flowchart in Fig. 7 for one 15-rotation sample being tested. It allows the statistics to be calculated for each blade separately as well as the data for the whole sample to be stored.

The population means and standard deviations σ are calculated for each blade by running the blade unloaded for 200 full-blade rotations at 16 rpm. For the misalignment tests, the blade was removed each time a new washer was added. The result of this is that after conducting the misalignment tests, the average displacements of the blades were altered significantly enough to cause error in the subsequent experiments. Therefore, new values of the population mean and standard deviation were calculated for the subsequent tests to give an accurate baseline for the hypothesis tests. These values are shown for the misalignment test and the subsequent tests in Tables 3 and 4, respectively, along with the number of datapoints collected for each blade. The datapoints are roughly 1500 per blade, which should be enough for the statistics calculated

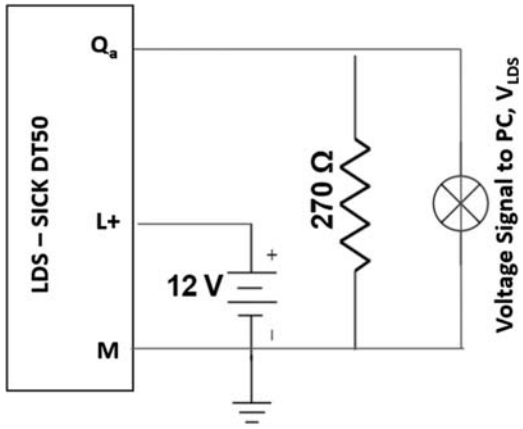

Fig. 6 Wiring diagram of the LDS

to be accurate representations of undamaged blade behavior. Blade 1 is the closest to the LDS sensor and blade 3 is the furthest.

To determine the optimal location for positioning the LDS, several different locations were tested. Previous studies [10] show that the displacement measured is higher at the tip, showing greater sensitivity for damage detection. For this paper, ten different locations near the tip, ranging from 100 mm to 10 mm from the tip, were tested to see which had the highest sensitivity. Tests are carried out for 40 cycles, both unloaded and with a 45 g mass attached at the root of blade 3. Then, the other tests were carried out on blade 1, on which the strain gauge was attached.

4 Results and Discussion

4.1 Strain Gauge. Figure 8 shows that the mean strain measured increases with each mass loading case for both the filtered and unfiltered strain tests. The increases are greater for the filtered case than the unfiltered, and this is also reflected in the z-values in Fig. 9. These show that the unfiltered samples have large negative spikes in strain, which are likely to bring the average strain down. These also occur for the filtered case but the figures show that they are about one order of magnitude smaller than the unfiltered case, meaning they have a less substantial effect. These spikes also only occur during loaded samples, suggesting that they are the cause of the increase in strain experienced. This explains the fact that the filtered samples have a lower standard deviation, as shown in Fig. 10.

Both filtered and unfiltered cases triggered the error for 99% significance for all the loading cases in this experiment, but because of all the improved sensitivity and the reduced noise, the filtered case is preferable for accurate and consistent use.

4.2 Laser Displacement Sensor

4.2.1 Location Tests. Figures 11–13 show the results of the location-determining tests described earlier in this report. Figure 11 shows that blades 1 and 3 get closer to the LDS but experience the least displacement change when mass is added to blade 3. Blade 2, which passes the LDS beam just before the loaded blade, has the largest change in displacement. This seems counter to what would be expected; one would expect that the loaded blade would experience the greatest change. This can be explained by the fact that the mass on blade 3 causes the blade hub, to which the blades are attached, to imbalance. This in turn will affect the positions of each of the attached blades in varying ways, dependent on where they are positioned relative to the loaded blade. The blade in front of it (blade 1) moves further away and the blade behind moves closer (blade 2).

Figure 11 shows R^2 values, which is a measure of the predictive capabilities of the linear model. It can be defined more precisely as

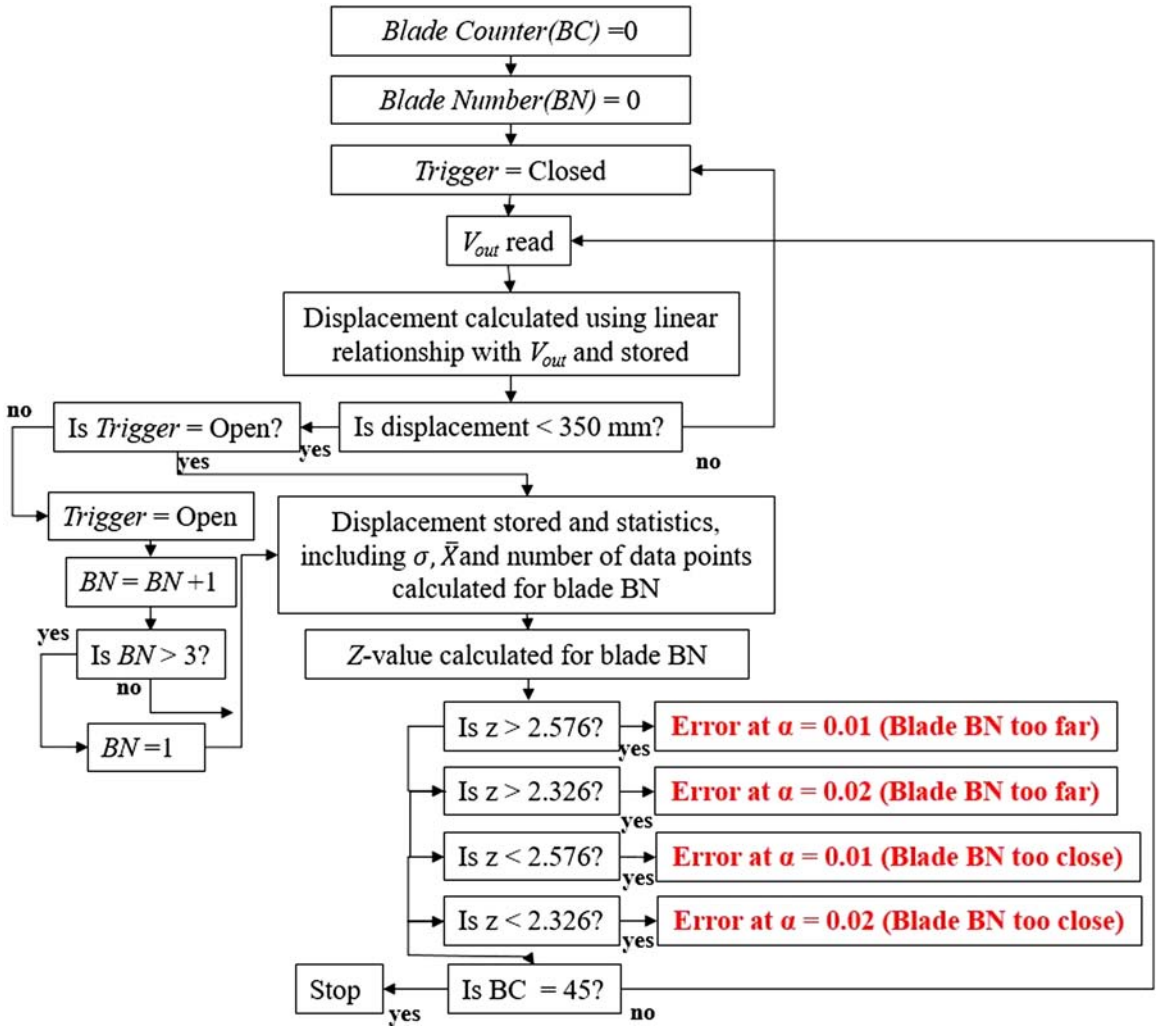

Fig. 7 Flow diagram showing the data processing and hypothesis testing that the VI runs for the strain gauge during one sample of 15 full-blade rotations

Table 3 Population means and standard deviations for each of the three blades on the turbine for the misalignment tests

Blade number	1	2	3
Population mean, μ_0	275.758	290.236	293.939
Population standard deviation, σ	6.433	3.933	3.256
Number of data points	1327	1216	1087

Table 4 Population means and standard deviations for each of the three blades on the turbine for the tests subsequent to the misalignment tests

Blade number	1	2	3
Population mean, μ_0	284.269	293.695	298.515
Population standard deviation, σ	17.1946	14.2622	13.1755
Number of data points	1522	1496	1430

the ratio between the variation explained by the model and the total variation.

Because of the extremely low R^2 values shown for blades 1 and 3 in Fig. 11, there can be no reliable conclusion based on the increase due to mass loading as the slight changes observed could be due to other factors such as the ±10 mm accuracy of the LDS.

As the LDS moves closer to the blade tip, the displacement measured increases for all blades, indicating the blades are further away. The standard deviation also reduces, indicating that variation due to LDS measuring inaccuracies is less likely. The standard deviation variations have low R^2 values, although they are on average slightly higher than for the mass loading increase. The displacement varies significantly along the length as shown in Figs. 14 and 15, with very high to quite high R^2 values, meaning the tip will be more sensitive to changes arising from damage. Therefore, the optimal location for the LDS sensor was determined to be nearest to the tip, at 10 mm away from the blade tip.

4.2.2 Misalignment Testing. Misalignment of blade 1 unsurprisingly causes an increase in displacement measured by the LDS, as shown in Fig. 17. The smallest misalignment of 0.6 mm caused an increase of 13 mm and—as Fig. 18 shows—a z-value roughly ten times the threshold for error. It can also be seen from Figs. 16 and 17 that, for some of the samples, blade 3 went below the lower threshold and blade 2 above the upper threshold, returning errors despite not being misaligned. This is due to the collateral effects of blade imbalance. Because the misaligned blade returned an error for all values of misalignment, the LDS and VI were successfully able to detect blade misalignment.

4.2.3 Bolt Loosening Testing. Bolt loosening has a similar effect on displacement to misalignment as shown in Fig. 18, although with a slightly weaker correlation ($R^2 = 0.824$ as opposed to 0.9474). One turn of the bolt was enough to trigger an

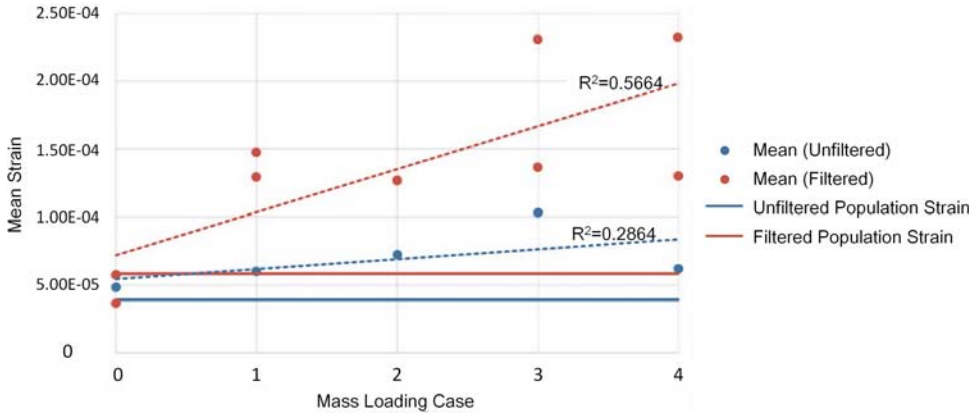

Fig. 8 Graph showing how the mean strain of 30 s samples changes with different mass loading cases for both filtered and unfiltered cases

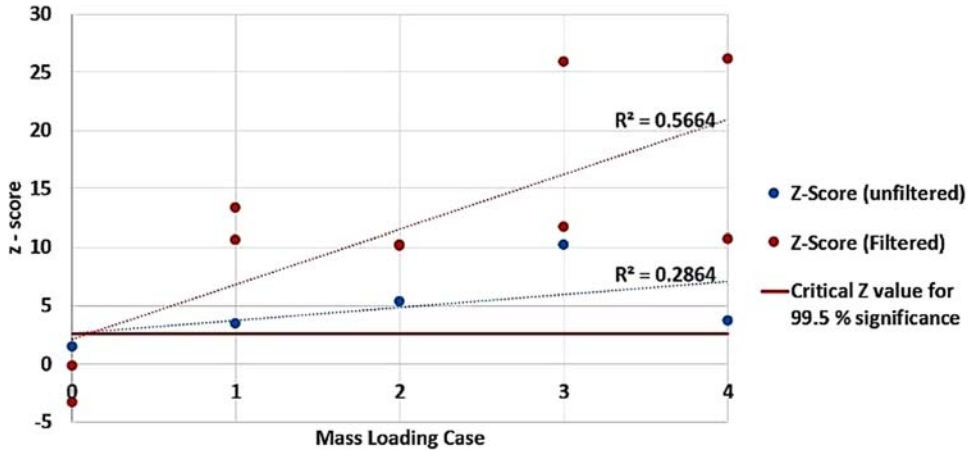

Fig. 9 Graph showing how the hypothesis test *z*-value of 30 s samples changes with different mass loading cases for both filtered and unfiltered cases

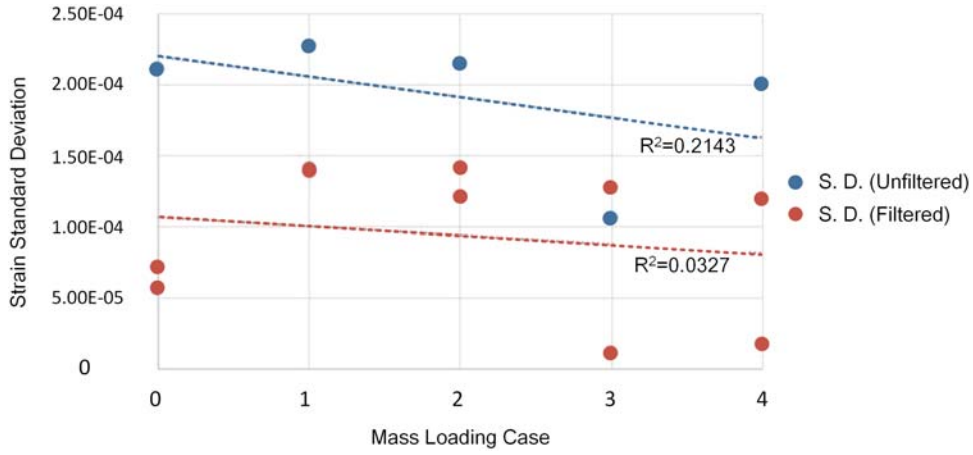

Fig. 10 Graph showing how the standard deviation of 30 s samples changes with different mass loading cases for both filtered and unfiltered cases

error warning with a *z*-value of 8.15 (Fig. 19). The other blades remained within the threshold to avoid triggering the error warning, which is what was desired.

The standard deviation of the loose blade decreases with the number of bolt turns, with an R^2 value of 0.909. This is much higher than with regular misalignment, where it decreases with an R^2 of 0.2. In order to distinguish between the two cases, the reliability of successive samples to lie on a predetermined linear model, as in Figs. 20 and 21, could be used.

4.2.4 Mass Loading Testing. The mass loading cases decreased the average displacement readings (Fig. 22) for blades

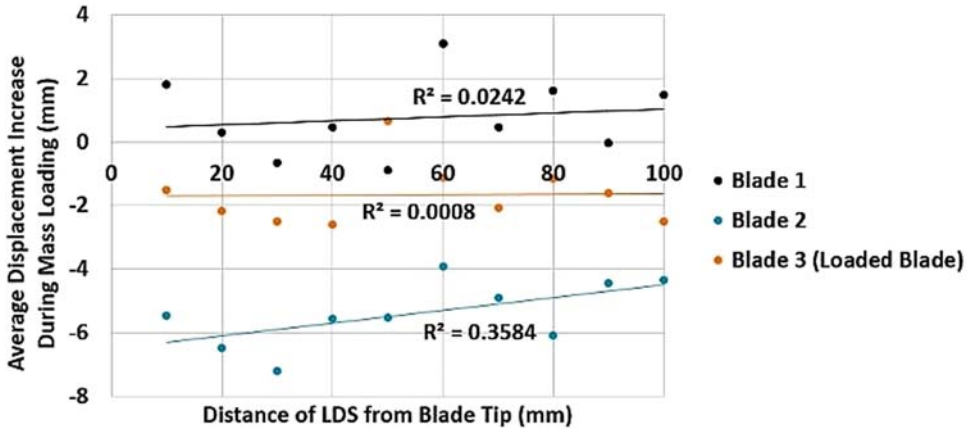

Fig. 11 Average displacement increase caused by loading near the blade tip measured for each blade

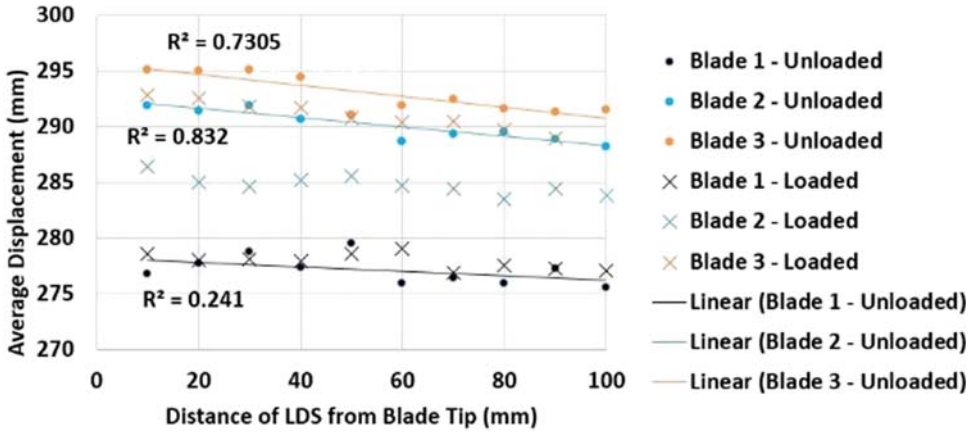

Fig. 12 Average displacement measured near the blade tip, measured for each blade

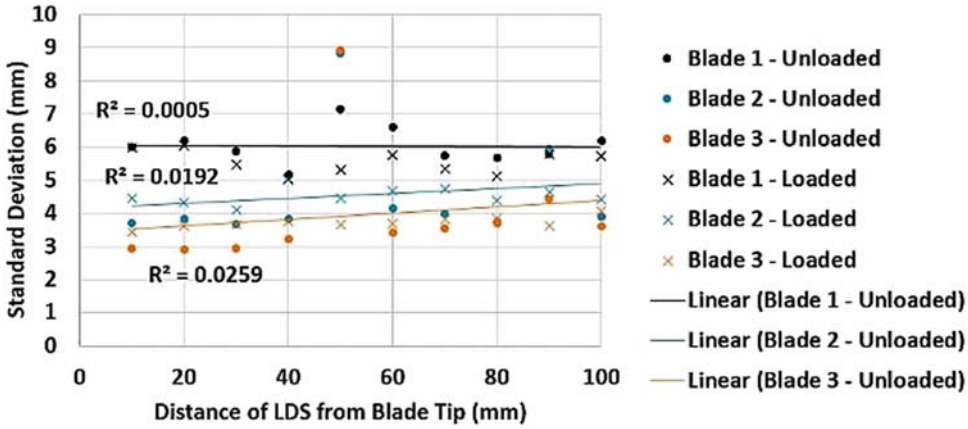

Fig. 13 Average standard deviation caused by loading near the blade tip, measured for each blade

1 and 2 but not for blade 3. This may be because when blade 2 is passing the tower, blade 1 is rising by the side of the tower, so the turbine is working against the extra weight of the blade and so will be more off balance for this time. This also explains the increase in average blade pass time during mass loading shown in Fig. 23 because the turbine will be running slower while blade 2 passes the LDS.

Despite the noticeable change in displacement during loading, the hypothesis test warning at 99% significance is only triggered for the two most severe loading cases 3 and 4, for which both blades 1 and 2 trigger warnings of being too close to the tower. This is shown in Figs. 24 and 25. An error was also detected for case 2 at the 98% significance level but not at the 99% significance level.

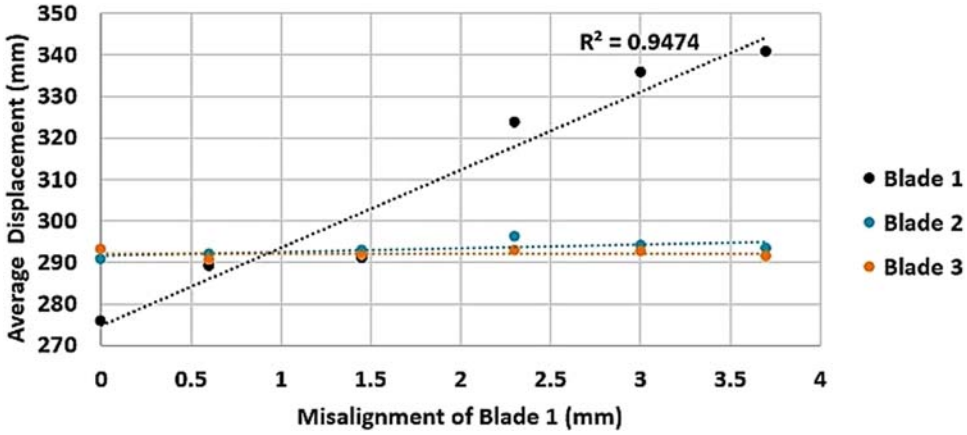

Fig. 14 Average displacement during different misalignments of blade 1

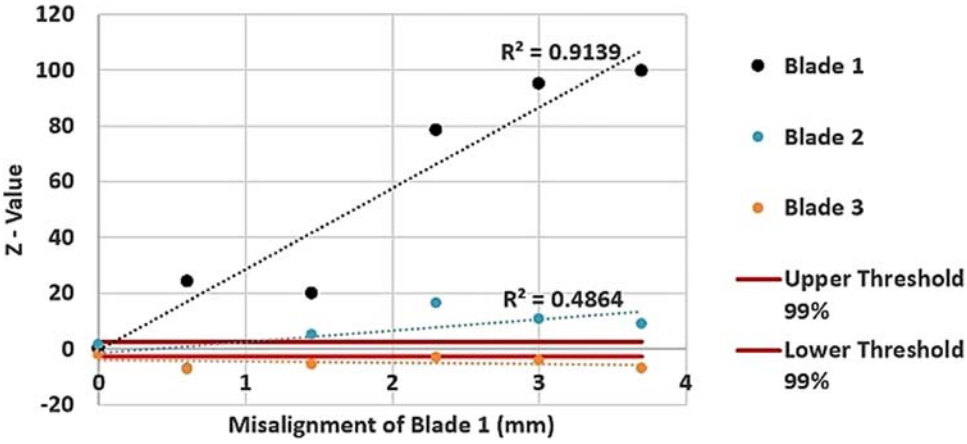

Fig. 15 Hypothesis test *z*-value during different misalignments of blade 1

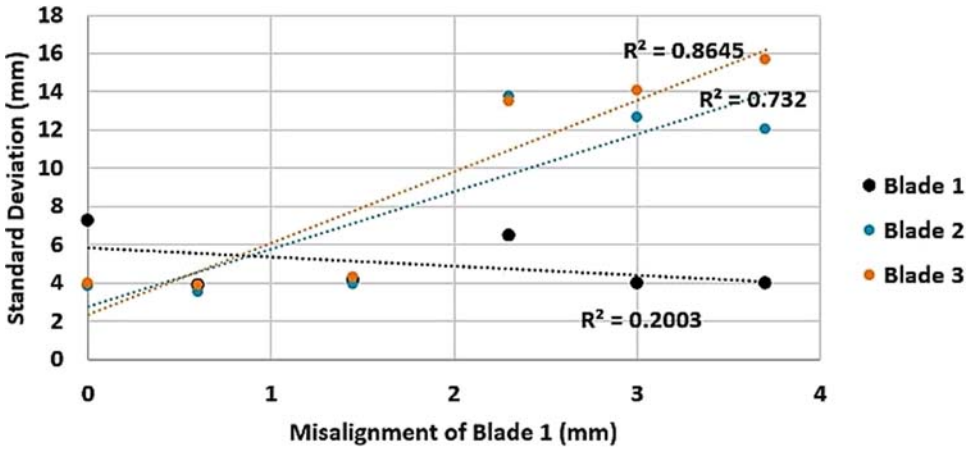

Fig. 16 Standard deviation variation during different misalignments of blade 1

If detection of less severe mass loading is required, then the VI could be adjusted to allow for this. For example, in this study, if a 95% significance level was chosen—with critical $z = 1.960$—then the mass loading case 1 would have been detected.

5 Conclusions

Experimentation proved the ability of a half-bridge type II strain gauge to detect ice loading to a 99% significance level in a lab environment. Similar tests are recommended to be carried out on full-scale WTs before recommendation for field use, but this experiment shows that these bridges have clear potential. Half-bridge type II gauges could be a cost-effective method of monitoring multiple WTs for mass loading during winter months.

A SICK DT-50 LDS was used to successfully detect, at a 99% significance level, misalignment of 0.6 mm and above and bolt loosening for one to three bolt turns. Of the mass loading cases

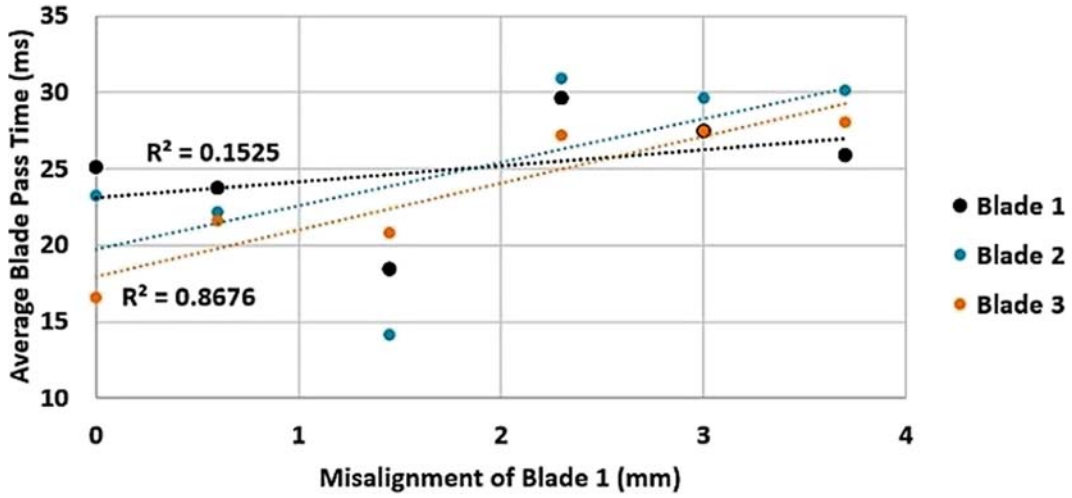

Fig. 17 Average blade pass duration during different misalignments of blade 1

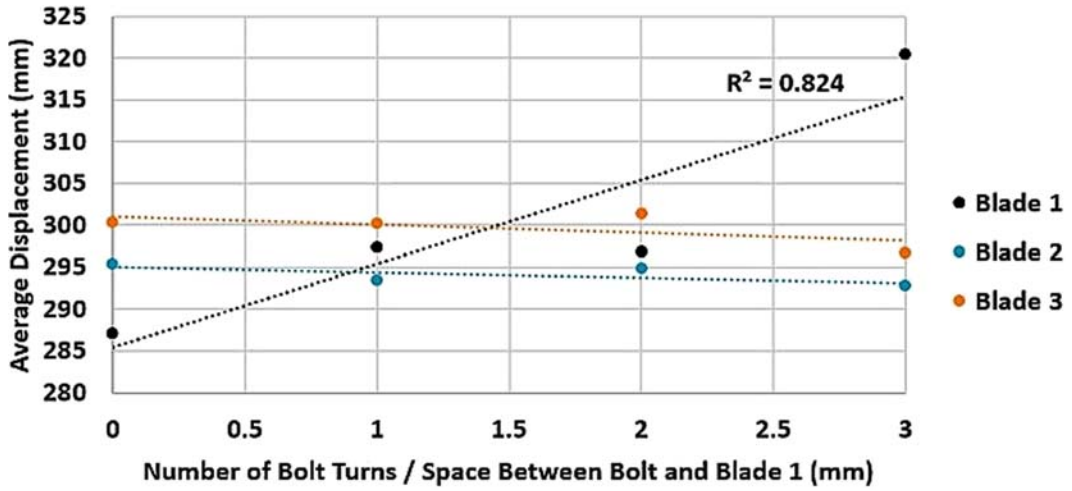

Fig. 18 Average displacement as the bolt on blade 1 is loosened incrementally

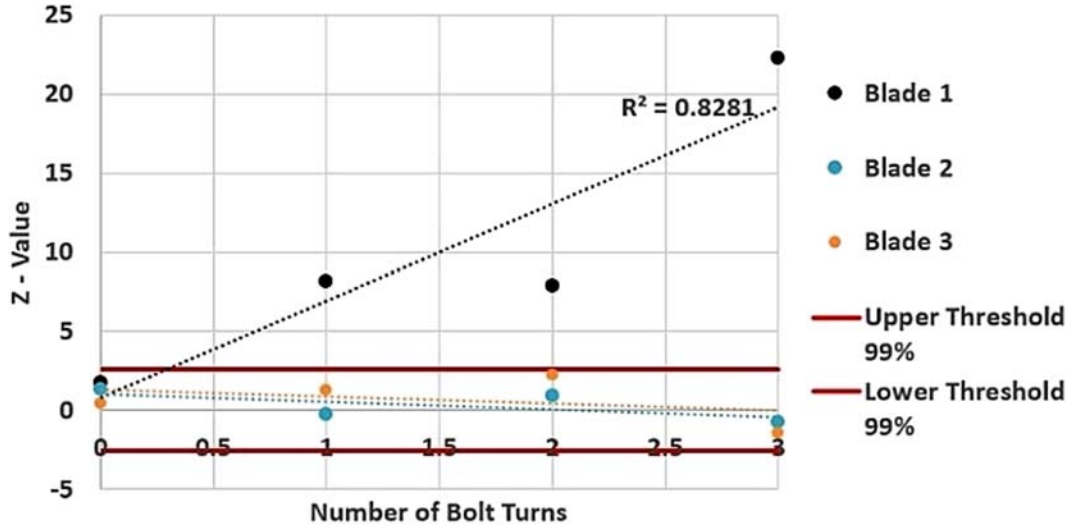

Fig. 19 Hypothesis test *z*-value as the bolt on blade 1 is loosened incrementally

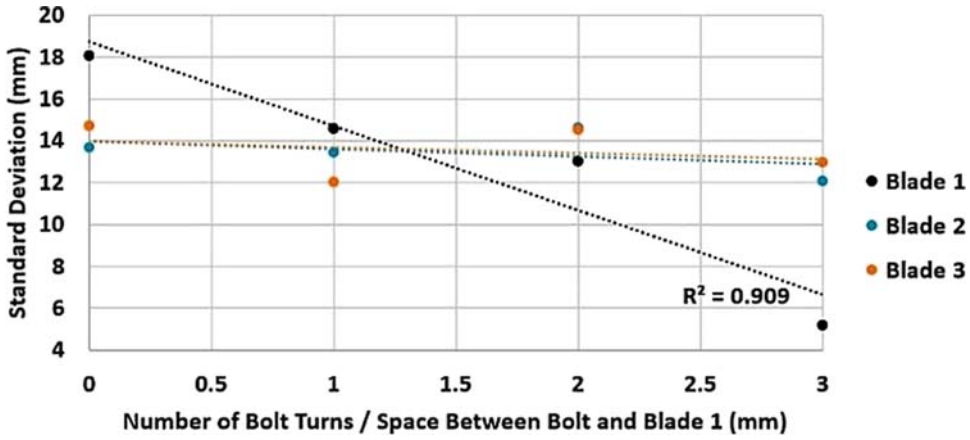

Fig. 20 Standard deviation as the bolt on blade 1 is loosened incrementally

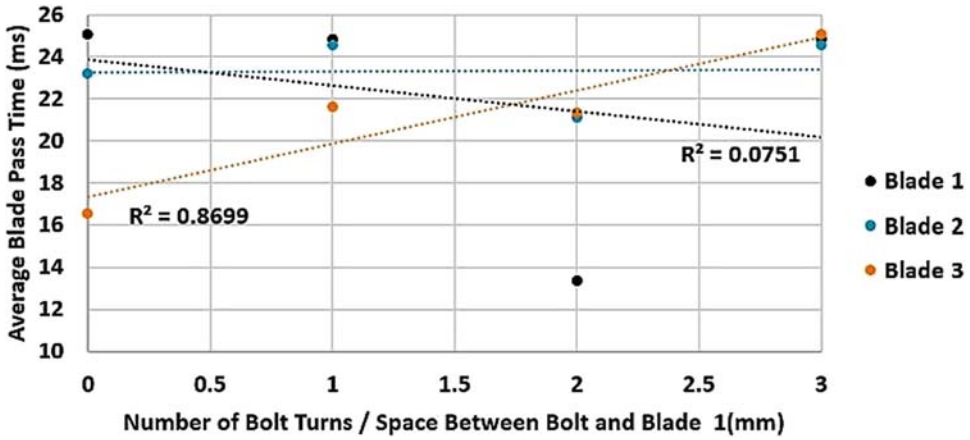

Fig. 21 Average blade pass time as the bolt on blade 1 is loosened incrementally

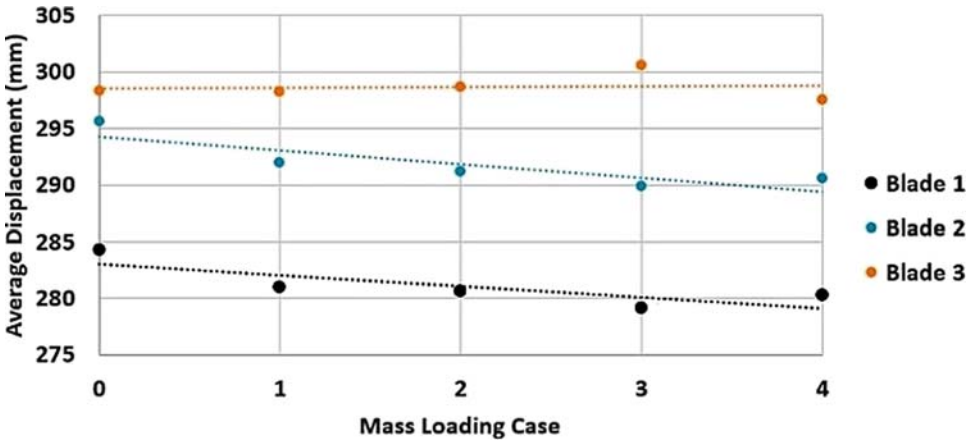

Fig. 22 Average displacement for different mass loading cases

tested with 11 g and 45 g masses, all were detected at 99% significance other than the case with 11 g at the root, which was detected at 98% significance. This shows that the LDS is capable of detecting smaller mass increases than previous studies [12–14]. With the LDS positioned as if it were inside the tower, unloaded blades were seen to be affected by the damaged blade, and these effects need to be considered when analyzing the data produced.

VIs were produced to give error warnings to an operator monitoring remotely, both in terms of strain and displacement. The strain gauge could detect more of the mass loading cases than the LDS, so they could be used in series for extra security.

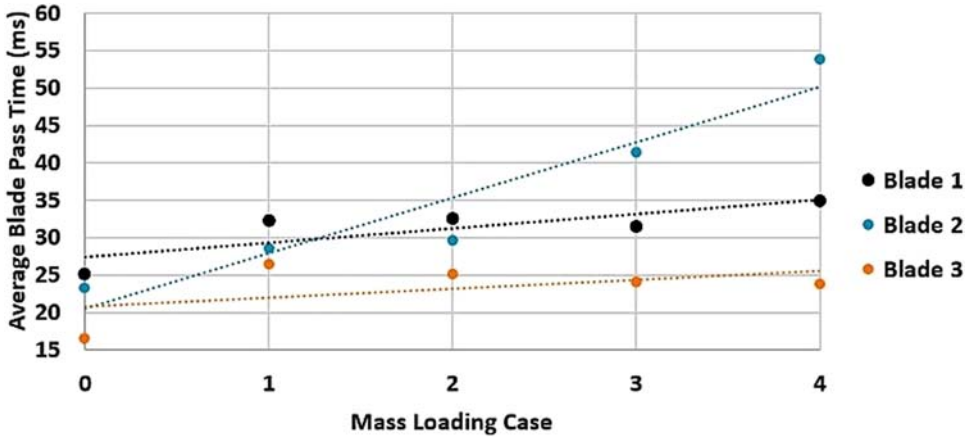

Fig. 23 Average blade pass duration for different mass loading cases

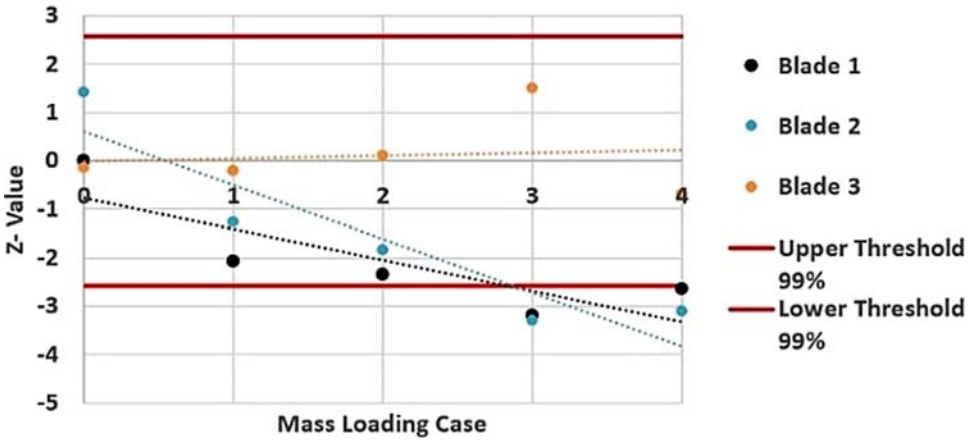

Fig. 24 Hypothesis test *z*-value for different mass loading cases

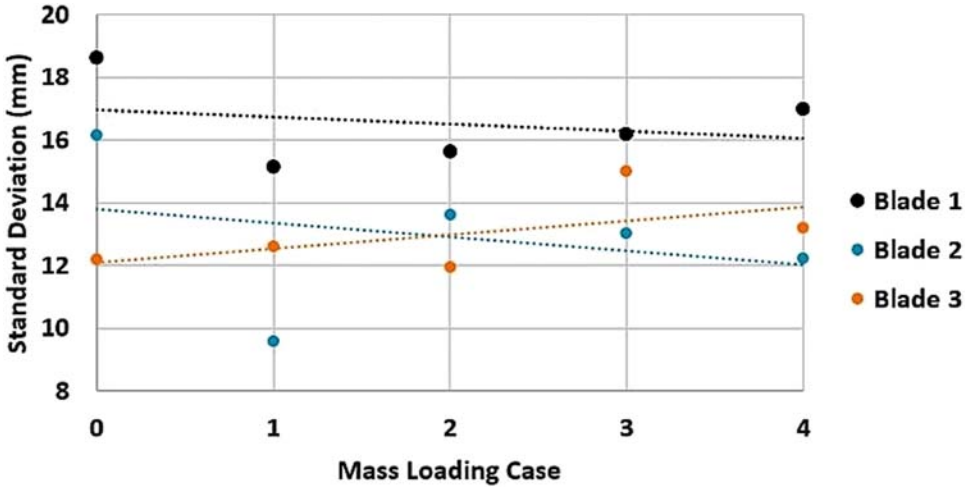

Fig. 25 Standard deviation for different mass loading cases

Acknowledgment

The work presented in this paper was supported by the Royal Academy of Engineering Newton Research Collaboration Programme Award under Award No. NRCP141591 (Funder ID: 10.13039/501100000287) and Distinguished Visiting Fellowship Award under Award No. DVF1415 2 17. Any opinions, findings, and conclusions or recommendations expressed in this publication are those of the authors and do not necessarily reflect the views of the Royal Academy of Engineering.

Nomenclature

d = displacement
n = sample size
L = original length
R = original resistance
$\bar{X}$ = sample mean
H_1 = alternative hypothesis
H_0 = null hypothesis
V_r = reference voltage
V_{out} = voltage output from the strain gauge
V_{ex} = strain gauge excitation voltage
GF = gauge factor
ΔL = change in lengths
ΔR = change in resistance
μ = actual population mean
μ_0 = assumed population mean
σ = population standard deviation
ε = strain

References

[1] Global Wind Energy Council, "Renewable Statistics," http://gwec.net/global-figures/graphs/. Accessed May 20, 2019.
[2] European Commission, "Renewable Energy Directive," https://ec.europa.eu/energy/en/topics/renewable-energy/renewable-energy-directive.
[3] Craig, C. C., Lee, J. R., and Bang, H.-J., 2008, "Structural Health Monitoring for a Wind Turbine System: A Review of Damage Detection Methods," Meas. Sci. Technol., **19**, p. 122001.
[4] Zhou, H. F., Dou, L. Z., Qing, L. Z., Chen, Y., Ni, Y. Q., and Ko, J. M., 2014, "A Review of Full-Scale Structural Testing of Wind Turbine Blades," Renew. Sust. Energ. Rev., **33**, pp. 177–187.
[5] Scientific American, "Offshore Wind Turbines Keep Growing in Size," https://www.scientificamerican.com/article/offshore-wind-turbines-keep/. Accessed May 20, 2019.
[6] Farrar, C. R., and Worden, K., 2007, "An Introduction to Structural," Philosophical Transactions of the Royal Society A: Mathematical, Physical and Engineering Sciences, **365**(1851), pp. 303–315.
[7] Moll, J., Arnold, P., Mälzer, K., Viktor, K., Pozdnizkov, D., Salman, R., Rediske, S., Scholz, M., Friedmann, H., and Nuber, A., 2018, "Radar-Based Structural Health Monitoring of Wind Turbine Blades: The Case of Damage Detection," Struct. Health. Monit., **17**(4), pp. 815–822.
[8] Wymore, M. L., Van Dam, J. E., Ceylan, H., and Qiao, D., 2015, "A Survey of Health Monitoring Systems for Wind Turbines," Renew. Sust. Energ. Rev., **52**, pp. 976–990.
[9] Berndt, M., Fellner, T., Zeiser, R., and Wilde, J., 2012, "Energy-Efficient Strain Gauges for the Wireless Condition Monitoring Systems in Mechanical Engineering," 6th European Workshop on Structural Health Monitoring - We.4.c.2, Dresden, Germany, July 2–6, pp. 1–9.
[10] Loraux, C., and Brühwiler, E., 2016, "The use of Long Term Monitoring Data for the Extension of the Service Duration of Existing Wind Turbine Support Structures," J. Phy. Conf. Ser., **753**, p. 072023.
[11] Kim, H., Giri, P., and Lee, J., 2013, "A Real-Time Deflection Monitoring System for Wind Turbines Blades Using a Built-in Laser Displacement Sensor," 6th European Workshop on Structural Health Monitoring - We.2.b.2, Dresden, Germany, July 2–6.
[12] Singh, J., 2014, *Real-Time Monitoring of Wind Turbine Blades Using Laser Measurement*, Durham University, Durham.
[13] Flanagan, O., 2016, *Real-Time Monitoring of Wind Turbine Blades Using Laser Displacement and Strain Measurement*, Durham University, Durham.
[14] Todd, T., 2017, *Real-Time Monitoring of Wind Turbine Blades Using Laser Displacement and Strain Measurement*, Durham University, Durham.
[15] Lee, J. R., and Kim, H. C., 2013, "Feasibility of In Situ Blade Deflection Monitoring of a Wind Turbine Using a Laser Displacement Sensor Within the Tower," Smart Mater. Struct., **22**(2), p. 027002.
[16] National Instruments, "Measuring Strain With Strain Gauges," http://www.ni.com/white-paper/3642/en/. Accessed May 20, 2019.
[17] Omega, "Strain Gauge Technical Data," https://www.omega.co.uk/techref/strain-gauge.html. Accessed May 20, 2019.
[18] National Instrument, "How is Temperature Affecting Your Strain Measurement Accuracy?" http://www.ni.com/white-paper/3432/en/. Accessed May 20, 2019.
[19] Bezziccheri, M., Castellini, P., Santolini, C., and Paone, N., 2017, "Measurement of Mechanical Loads in Large Wind Turbines: Problems on Calibration of Strain Gauge Bridges and Analysis of Uncertainty," Wind Energy, **20**(2), pp. 1997–2010.
[20] Papadopoulos, K., Morfiadakis, E., Philippidis, T. P., and Lekou, D. J., 2000, "Assessment of the Strain Gauge Technique for Measurement of Wind Turbine Blade Loads," Wind Energy, **3**(1), pp. 35–65.
[21] Aihara, A., Kawaguchi, T., Miki, N., Azami, T., Sakamoto, H., and Okuma, M., 2017, "A Vibration Estimation Method for Wind Turbine Blades," Exp. Mech., **57**(8), pp. 1213–1224.
[22] Lee, K., Aihara, A., Puntsagdash, G., Kawaguchi, T., Sakamoto, H., and Masaaki, O., 2017, "Feasibility Study on a Strain Based Deflection Monitoring System for Wind Turbine Blades," Mech. Syst. Signal Process., **82**, pp. 117–129.
[23] National Instruments, "FBG Optical Sensing: A New Alternative for Challenging Strain Measurements," http://www.ni.com/white-paper/12338/en/. Accessed May 20, 2019.
[24] Allwood, G., Wild, G., and Hinckley, S., 2017, "Fiber Bragg Grating Sensors for Mainstream Industrial Processes," Electronics, **6**(92), pp. 2–19.
[25] Mieloszyk, M., and Ostachowicz, W., 2017, "An Application of Structural Health Monitoring System Based on FBG Sensors to Offshore Wind Turbine Support Structure Model," Mar. Struct., **51**, pp. 65–86.
[26] Park, S., Park, T., and Han, K., 2011, "Real-time Monitoring of Composite Wind Turbine Blades Using Fiber Bragg Grating Sensors," Adv. Compos. Mater., **20**(1), pp. 39–51.
[27] Boston Piezo Optics Inc, "Piezoelectric Components," http://www.bostonpiezooptics.com/intro-to-transducer-crystals. Accessed May 20, 2019.
[28] HBM, "Piezoelectric or Strain Gauge Based Force Transducers?," https://www.hbm.com/en/3719/piezoelectric-or-strain-gauge-based-force-transducers/. Accessed May 20, 2019.
[29] Lim, D. W., Mantell, S., and Seiler, P., 2016, "Wireless Monitoring Algorithm for Wind Turbine Blades Using Piezo-Electric Energy Harvesters," Wind Energy, **20**(3), pp. 551–565.
[30] Southwest Windpower Inc. "*Air Breeze Owner's Manual*," Flagstaff, AZ.
[31] The Pennsylvania State University, "Z-Test: When Population Variance is Known," https://onlinecourses.science.psu.edu/stat414/node/269. Accessed May 20, 2019.
[32] OMEGA Engineering, "Practical Strain Gauge Measurements," https://www.omega.co.uk/techref/pdf/StrainGaugeCalcs.pdf. Accessed May 20, 2019.
[33] National Instruments, "Engineer's Guide to Accurate Sensor Measurements," https://www.eenewsanalog.com/Learning-center/national-instruments-engineers-guide-accurate-sensor-measurements. Accessed May 20, 2019.
[34] Sick Sensor Intelligent, "DT50-P1113 Online Data Sheet," https://www.sick.com/media/pdf/4/64/264/dataSheet_DT50-P1113_1044369_en.pdf. Accessed May 20, 2019.